Available online at www.sciencedirect.com
ScienceDirect
International Journal of Heat and Mass Transfer 50 (2007) 4206–4218
International Journal of HEAT and MASS TRANSFER
www.elsevier.com/locate/ijhmt

Subsonic compressible flow in two-sided lid-driven cavity. Part I: Equal walls temperatures

P. Shah [a], B. Rovagnati [a], F. Mashayek [a,*], G.B. Jacobs [b]

[a] Department of Mechanical and Industrial Engineering, University of Illinois at Chicago, 842 West Taylor Street, Chicago, IL 60607, United States
[b] Department of Aerospace Engineering and Engineering Mechanics, San Diego State University, San Diego, CA 92182, United States

Received 2 January 2007; received in revised form 16 February 2007
Available online 3 May 2007

Abstract

This paper presents a numerical study of the laminar, viscous, subsonic compressible flow in a two-dimensional, two-sided, lid-driven cavity using a multi-domain spectral element method. The flow is driven by steadily moving two opposite walls vertically in opposite directions. All the bounding walls have equal temperatures. The results of the simulations are used to investigate the effects of the cavity aspect ratio, the Reynolds number and the Mach number on the flow. At lower Reynolds numbers, the flow pattern consists of two separate co-rotating vortices contiguous to the moving walls. For higher Reynolds numbers, initially a two-vortex flow is formed, which eventually turns into a single elliptical vortex occupying most of the cavity. For a higher aspect ratio, the flow patterns are dissimilar in that the streamlines become more and more elliptic. For aspect ratios as high as 2.5, at high Reynolds numbers, a three-vortex stage is formed. It is found that the compressibility effects are not very significant for Mach numbers less than 0.4. Dissipation of kinetic energy into internal energy changes the temperature field especially near the boundaries. Boundary layer studies suggest that the velocity and temperature boundary layer thicknesses are lower for higher Reynolds numbers. For engineering purposes, these thicknesses can be approximated by the existing flat-plate solutions.

1. Introduction

This paper presents a numerical investigation of the subsonic compressible laminar flow in a two-sided lid-driven cavity using a multi-domain spectral element method. The fluid flow in a closed cavity driven by tangentially moving walls in opposite directions is a benchmark flow geometry for testing numerical techniques. The flow enclosed in a simple bounded domain comprises of crucial wall effects, yet, any geometrical impediments are absent.

In the classical problem of one-sided lid-driven cavity [1], one of the sidewalls is moving either steadily or in a time-dependent manner tangentially to itself. This configuration has been considered comprehensively, both experimentally and numerically [2]. In recent years, the flow induced by the motion of two opposite walls in antiparallel directions, i.e. the two-sided lid-driven cavity flow, has also been explored [3,4]. This configuration is considered in this work for a subsonic compressible flow.

A review of all the studies on the one-sided lid-driven cavity would exceed the scope of this work. An excellent review on the single-lid-driven cavity has been provided by Shankar and Deshpande [5] in which the large variety of incompressible flow phenomena in the lid-driven cavity are summarized as eddies, secondary flows, complex three-dimensional (3D) patterns [6], chaotic particle motions, instabilities, transition, and turbulence. Here, we provide a brief review of previous works. Lid-driven cavity flows have been studied both experimentally and numerically for several years. Some of the key investigations into the lid-driven cavity flow include the first major research in the setting of steady two-dimensional one-sided lid-driven cavity flow by Burggraf [1] for a square cavity and by Pan and Acrivos [7] for other geometrical aspect ratios.

* Corresponding author. Tel.: +1 312 996 1154; fax: +1 312 413 0447.
E-mail address: mashayek@uic.edu (F. Mashayek).

0017-9310/$ - see front matter © 2007 Elsevier Ltd. All rights reserved.
doi:10.1016/j.ijheatmasstransfer.2007.02.028

Nomenclature

c	$\sqrt{p\gamma/\rho}$ speed of sound
c_p	constant pressure specific heat of the fluid
c_v	constant volume specific heat of the fluid
F	flux vector in x-direction
G	flux vector in y-direction
h	convective heat transfer coefficient
L	length
L_f	reference length
$L_{w,top}$	length of the top wall
$L_{w,bottom}$	length of the bottom wall
$L_{w,left}$	length of the left wall
$L_{w,right}$	length of the right wall
L_h	length of the horizontal walls
L_v	length of the vertical walls
M_f	$U_f^*/\sqrt{\gamma R^* T_f^*}$ reference Mach number
Ma	$uM_f/\sqrt{T}$ Mach number
p	$\rho T/\gamma M_f^2$ pressure of the fluid
Pr	$c_p^*\mu^*/\kappa^*$ Prandtl number
q	heat flux
$\vec{Q}$	vector of solution unknowns
R	gas constant
Re	$\rho^* U^* L^*/\mu^*$ Reynolds number
Re_f	$\rho_f^* U_f^* L_f^*/\mu^*$ reference Reynolds number
t	time
T	temperature
T_f	reference temperature
T_i	initial temperature
$T_{w,left}$	temperature of the left wall
$T_{w,right}$	temperature of the right wall
u, v	velocity of the fluid in x and y directions, respectively
V_{wall}	wall velocity
$V_{w,left}$	velocity of the left wall
$V_{w,right}$	velocity of the right wall
U_f	reference velocity
x, y, z	spatial coordinates
w	depth of the cavity in z-direction

Greek symbols

γ	ratio of the specific heats of the fluid
Γ	aspect ratio of the cavity
δ	boundary layer thickness
δ_V	velocity boundary layer thickness
δ_T	thermal boundary layer thickness
κ	thermal conductivity
μ	dynamic viscosity
ρ	density
τ	stress tensor

Subscripts

i	initial
f	reference variable
t, x, y	derivative with respect to variable t, x and y, respectively

Superscripts

–	averaged quantity
→	vector
*	physical space variable
a	advective flux
v	viscous flux

Pan and Acrivos [7] showed that the two-dimensional cavity flow eddy structure in a rectangular cavity is highly dependant on the aspect ratio. These two-dimensional patterns were, however, not observed experimentally [7]. In fact, until 1984, most of the experimental studies did not model the same flow that was of interest to the numerical investigators, i.e., a flow driven by a flat impermeable lid [8]. For example, Pan and Acrivos [7] performed visualization of a cavity flow driven by a circular cylinder, and the experiments of Bogatyrev and Gorin [9] were typical of cavity experiments conducted in channel cutouts where the lid was the overlying stream of fluid, leading to mixing between the fluid in the cavity and the external stream. A desire to learn more about the physics of lid-driven cavity flows and the need for a benchmark solution for numerical modelers prompted a set of experiments by Koseff and Street [2,10,11] who confirmed the flow patterns predicted numerically. The findings of Pan and Acrivos [7] were later extended by Goodrich et al. [12] and Shen [13] who numerically calculated the transition to time-dependent two-dimensional cavity flows. Motivated by the application to coating processes, a variant of one-sided rectangular lid-driven cavity was investigated by Aidun et al. [14] and Benson and Aidun [15]. Aidun et al. [14] showed that cavity flows were directly relevant to coaters and generalized cavity flows as dynamical systems.

The one-sided lid-driven cavity problem was generalized to the two-sided lid-driven cavity problem by Kuhlmann et al. [3]. They investigated two- and three-dimensional flows experimentally and numerically for different aspect ratios and Reynolds numbers. In addition to their identification of the hydrodynamic stability and pattern formation, they found that the two-sided lid-driven cavity is well-suited for the study of viscous corner eddies [16,17] and the corner singularity [18]. Kelmanson and Lonsdale [19] and Brons and Hartnack [20] found that in a two-sided lid-driven cavity, when the flow field changes due to unsteadiness of the flow or an external change of parameters or boundary conditions, the streamline topology may also change. They also found that when the flow field is varied through a degenerate configuration that is structurally unstable, the streamline pattern can bifurcate and new

structures arise away from the boundaries. Only recently, a three-dimensional linear stability analysis of the two-dimensional cavity flow with periodic boundary conditions in the spanwise direction has been carried out by Albensoeder and Kuhlmann [6].

A description of the self-similar structure of the eddies near the corners was given by Moffat [21], Pan and Acrivos [7], and Kelmanson and Lonsdale [19]. A physical description of the mechanism for the formation of the corner eddies was given in Ref. [2]. They found that when the wall jet, that forms on the downstream wall of the cavity, encounters the pressure gradient induced by the corner, separation occurs, resulting in the formation of a secondary eddy in the corner. Koseff and Street [11] and Prasad and Koseff [8] found that the flow in a lid-driven cavity is strongly affected by aspect ratio of the cavity and that this effect is different for low and high Reynolds numbers. The recent experiments of Migeon et al. [22] and Guermond et al. [23] focused on the transient development of cavity flows. They concluded that the shallower the cavity, that is larger the aspect ratio, the sooner the pressure gradient imposed by the depth of the cavity was felt by the growing corner vortex and the sooner steady state was reached.

The previous studies of two-sided lid-driven cavity are focused on steady state flows. In this work, we study the temporal evolution of this flow, in which we also include the compressibility effects. Some practical applications of a two-sided lid-driven cavity suggest that compressibility effects may be significant to the flow. Yet, although this flow has been studied extensively, the compressibility effects have never been taken into consideration. A further extension of the present work (Part II, Ref. [24]) will be to study the effect of different walls temperatures, as it is of great interest in applications such as coating and drying processes. There, the boundary conditions will be modified from a homogenous temperature boundary condition domain to a higher temperature at one of the moving walls and a lower temperature at the other moving wall compared to the initial temperature.

In the next section, the governing equations and numerical method are presented. Section 3 is dedicated to discussions of the flow for cases with different Reynolds numbers, aspect ratios, and Mach numbers, respectively. Finally, concluding remarks are provided in Section 4.

2. Formulation and methodology

We consider the two-dimensional, two-sided lid-driven cavity flow with initially uniform temperature T_i and all the four surrounding walls at rest as shown in Fig. 1. The velocity boundary conditions are employed on the two vertical walls, by giving them the same magnitude of velocity V_{wall}, but in opposite directions in order to have anti-parallel wall motion, i.e. $V_{w,right} = -V_{wall}$ and $V_{w,left} = V_{wall}$. The u velocity component for the moving walls is zero. We refer to the two moving walls as the left and right moving walls. Therefore, since the temperatures of the moving and stationary walls are the same as the initial temperature, the temperature boundary conditions can be written as $T_{w,right} = T_{w,left} = T_i$.

For the rectangular cavity, the horizontal and vertical wall lengths are defined as, $L_{w,top} = L_{w,bottom} = L_h$ and $L_{w,left} = L_{w,right} = L_v$. The length of the vertical or moving walls L_v is the reference length and the aspect ratio $\Gamma = L_h/L_v$ of the domain is changed by changing the length of the horizontal or stationary walls L_h. We take $\Gamma \geqslant 1$ for all our simulations.

We deal with the subsonic region of the compressible fluid flow. Throughout the domain, the Mach number is always kept less than 0.8, so as not to venture into the transonic region in order to avoid shocks. If two opposite walls moving in anti-parallel motion drive the flow, the resulting flow pattern is not unique. A multitude of flow patterns are expected to occur. The flow structures depend sensitively on the aspect ratio of the cavity, the boundary conditions and the Reynolds number. The effect of these parameters on flow pattern is investigated in detail in this work and in Part II [24].

2.1. Governing equations

We assume a Newtonian ideal gas with zero bulk viscosity. The heat flux obeys the Fourier's law, and the viscosity, thermal conductivity and specific heats of the gas are

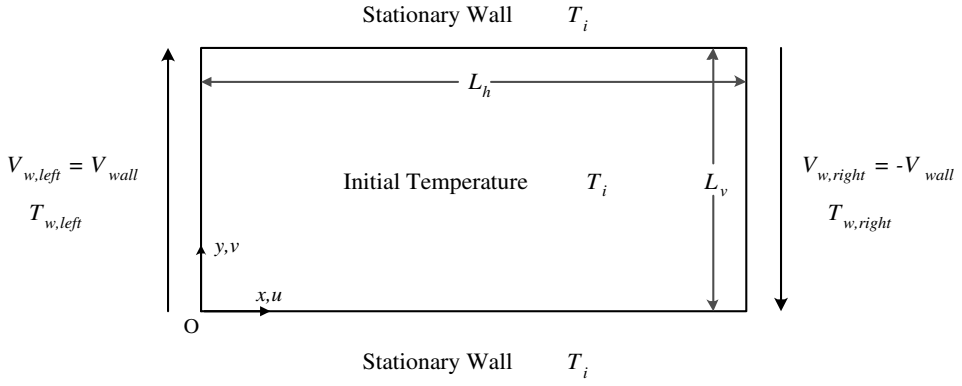

Fig. 1. Schematic diagram of the two-sided lid-driven cavity.

assumed to be independent of temperature. For numerical solution of the Navier Stokes equations, the dimensional form is not favored, since the disparity of the physical variables can generate undesirable errors. Therefore, all variables are non-dimensionalized by reference scales of length $L_f^* = L_v$, velocity $U_f^* = V_{wall}$, temperature $T_f^* = T_i$, and density ρ_f^* taken as the constant density of the gas. This leads to the following non-dimensional continuity, momentum and energy equations

$$\vec{Q}_t + \vec{F}^a_x + \vec{G}^a_y = \frac{1}{Re_f}(\vec{F}^v_x + \vec{G}^v_y), \tag{1}$$

where

$$\vec{Q} = \begin{bmatrix} \rho \\ \rho u \\ \rho v \\ \rho e \end{bmatrix}, \quad \vec{F}^a = \begin{bmatrix} \rho u \\ p + \rho u^2 \\ \rho uv \\ u(\rho e + p) \end{bmatrix}, \quad \vec{G}^a = \begin{bmatrix} \rho v \\ \rho uv \\ p + \rho v^2 \\ v(\rho e + p) \end{bmatrix}, \tag{2}$$

and

$$\vec{F}^v = \begin{bmatrix} 0 \\ \tau_{11} \\ \tau_{12} \\ u\tau_{11} + v\tau_{12} + T_x/(\gamma - 1)M_f^2 Pr \end{bmatrix},$$

$$\vec{G}^v = \begin{bmatrix} 0 \\ \tau_{21} \\ \tau_{22} \\ u\tau_{21} + v\tau_{22} + T_y/(\gamma - 1)M_f^2 Pr \end{bmatrix}, \tag{3}$$

with,

$$\tau_{11} = 2[u_x - (u_x + v_y)/3],$$

$$\tau_{22} = 2[v_y - (u_x + v_y)/3], \quad \tau_{12} = v_x + u_y. \tag{4}$$

The total energy per unit volume is given as

$$\rho e = \frac{p}{\gamma - 1} + \rho(u^2 + v^2)/2. \tag{5}$$

In Eqs. (3) and (4) the subscript on the stress tensor, τ, defines the direction of τ and the plane it is acting on, whereas the subscripts x and y on u, v and T indicate derivatives. The non-dimensionalization gives rise to three non-dimensional numbers. The reference Reynolds number, Re_f, which indicates the influence of the viscous fluxes as compared to the advective fluxes, the Prandtl number, Pr, which is the ratio of the momentum and thermal diffusivities, and the reference Mach number M_f. In this work, M_f is taken equal to unity, such that the reference velocity is equal to the reference speed of sound, and $Pr = 0.72$ is used. Finally, the ideal gas equation of state in non-dimensional form is given by

$$p = \frac{\rho T}{\gamma M_f^2}. \tag{6}$$

2.2. Numerical considerations

The governing equations are solved using a multi-domain, staggered-grid, Chebyshev, spectral element code which has been developed and extensively tested by our group [25–27]. Standard Chebyshev spectral methods, like all other spectral methods, applied to compressible flow problems have some severe restrictions. The computational domain must be simple enough to map onto a square in two space dimensions, or a cube in three. In some cases, to increase spatial resolution, the polynomial approximation order must be increased. For high orders, the derivative approximations must be performed with fast Fourier transform methods in order to be efficient. In many cases, if matrix multiplication is used instead, the computational work grows too rapidly with the number of degrees of freedom to be practical. The basic premise of a multi-domain method is that these restrictions can be reduced by subdividing the computational domain into multiple zones, called sub-domains, on which the spectral approximation is applied. As a result, the method can be used on more complex geometries. The use of lower order approximating polynomials in each sub-domain means that matrix multiplication can be both efficient and accurate. For more detail discussions of the method we refer to Refs. [25–27].

The discontinuity of the boundary conditions in the corners between the stationary and moving boundaries requires special treatment. To overcome this difficulty, Kuhlmann et al. [3] used smoothing in these corners. In this study, the following boundary conditions are used in order to regularize the problem

$$v = \begin{cases} \frac{1-y}{0.05} & \text{if} \quad y > 0.95, \\ 1 & \text{if} \quad 0.05 \leqslant y \leqslant 0.95, \\ \frac{y}{0.05} & \text{if} \quad y < 0.05, \end{cases} \tag{7}$$

at $x = 0$, and

$$v = \begin{cases} -\frac{1-y}{0.05} & \text{if} \quad y > 0.95, \\ -1 & \text{if} \quad 0.05 \leqslant y \leqslant 0.95, \\ -\frac{y}{0.05} & \text{if} \quad y < 0.05, \end{cases} \tag{8}$$

at $x = \Gamma$.

A comprehensive grid resolution and temporal convergence study has been conducted. The results of this study are reported in Ref. [28] and are not shown here for brevity. A non-uniform grid with 80 spectral elements and polynomial orders of 6, 8 and 10, resulting in 2880, 5120 and 8000 cells, respectively, is used. The grid is compressed near the walls and stretched towards the center of the cavity. A quantitative comparison of the steady state converged results obtained from the spectral element code is conducted with published results ([3], private communication) for incompressible flow for a case with equal wall temperature boundary condition, $\Gamma = 1.955$, $Ma = uM_f/\sqrt{T} =$

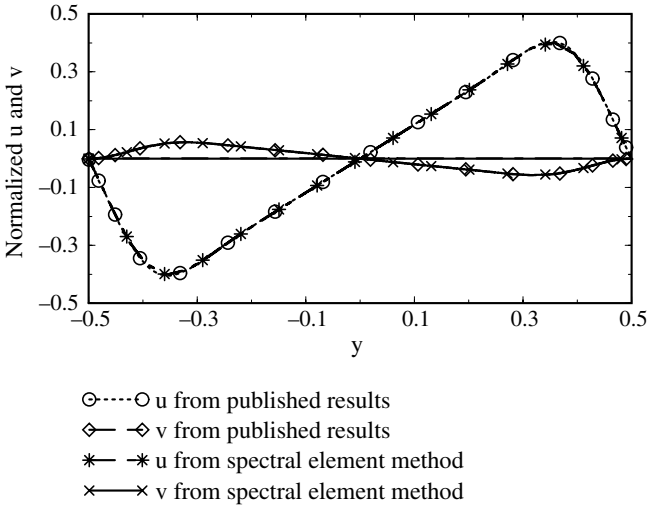

Fig. 2. Comparison with published numerical results for $Re = 700$.

0.4, and $Re = 800$. The comparisons of the results are shown in Fig. 2 for u and v along the vertical centerline $x = 0.5$. The results form spectral element method obtained with 2880 cells are compared with those from Ref. [3] calculated with a total number of 19,881 cells. The published results used for comparison here are calculated using a second-order finite difference method on an equidistant grid in the y-direction and a Chebyshev collocation method on Gauss–Lobatto points in the x-direction.

When the curves of u and v velocity components at steady state are superposed, it is seen that the center of the vortex formed, is at the zero velocity point i.e. the center of the rectangular domain. (Note that the velocities and the y coordinate in Fig. 2 are normalized according to the published results.) This comparison shows excellent agreement with previously published results. From Fig. 2, it can be concluded that a flow at Mach number of 0.4 shows the same velocity field as compared to incompressible flow with all other specifications the same. Simulations conducted for other Mach numbers suggest that the streamline topologies do not depend on Mach number for $Ma \leqslant 0.4$ for the two-sided lid-driven cavity.

3. Results

3.1. Flow evolution

We begin our discussion of the results by considering the flow evolution for a case with $Re = 700$, $\Gamma = 1.955$ and $Ma = 0.4$. The two walls are moving in anti-parallel directions with the same temperature boundary conditions. This particular combination of $Re = 700$ and $\Gamma = 1.955$ is selected in order to study the merging of the two vortices that are formed near the moving walls. For the range of Reynolds numbers lower than or equal to 400, the steady state result is a two-vortex state, as the two smaller vortices formed near the center of the stationary walls do not have enough strength to push the larger vortices to combine. For a higher Reynolds number of $Re = 700$, flow evolves somewhat differently because of the increase in the strength of these vortices.

Initially the temperature is constant throughout the domain, the walls are at rest, and all the velocities are zero. A simulation is conducted for this case until the flow reaches a steady state. The streamlines in Fig. 3a–f show different flow stages with time. Shear stress is exerted by the moving walls on the fluid, and due to viscosity, there is shear stress between the layers of fluid. This leads to friction which eventually causes dissipation of heat due to which the temperature in the domain changes. A temperature field thus develops due to a velocity field. The streamlines in Fig. 3 are colored by temperature in order to study the temperature field change along with the velocity field change.

Due to the movement of the walls, two vortices are formed adjacent to the moving walls. There is also the formation of two smaller vortices in the middle of the domain, near the stationary walls, due to the inherent tendency of the two bigger vortices formed by the moving walls to stay circular. The clockwise direction of rotation of the two bigger vortices is according to the respective moving walls which direct them. The direction of rotation of the two smaller vortices is counter-clockwise because of the coupled effect of the two moving larger vortices. Also, all the four vortices try to shift in clockwise direction. The smaller vortices have a very high magnitude of vorticity of the order of 300 units compared to the larger vortices which have the magnitude of vorticity of the order of 30. The smaller vortices thus, push the larger vortices in order to move in the clockwise direction. Again, the two larger vortices have a propensity of remaining in a circular shape. As time passes, these vortices gain more and more strength, and tend to become larger. However, due to the bounding walls and the two smaller vortices pushing them away from the trailing edges of the moving walls, they have a limitation of growing. The aspect ratio of 1.955 allows the vortices to come close enough and merge in the end giving rise to a single stronger elliptical vortex. Meanwhile, the two smaller vortices in the center move towards the corners as this merging is taking place. These smaller vortices increase in size because of the space now available. The smaller vortices are now close to the respective walls but have counter-clockwise direction which is opposite to the direction of rotation of the two walls. Meanwhile, the center of the larger vortex now is at the center of the cavity and it tries to become circular by pushing the smaller ones to decrease in size. Their sizes decrease with time as the flow enters the steady state regime. Thus, at steady state, the elliptical vortex formed after the combination of the two initial vortices occupies most of the cavity and the size of the two smaller vortices decreases comparatively. It should be noted here, that the two smaller vortices which loose their strength at steady state for a Reynolds number

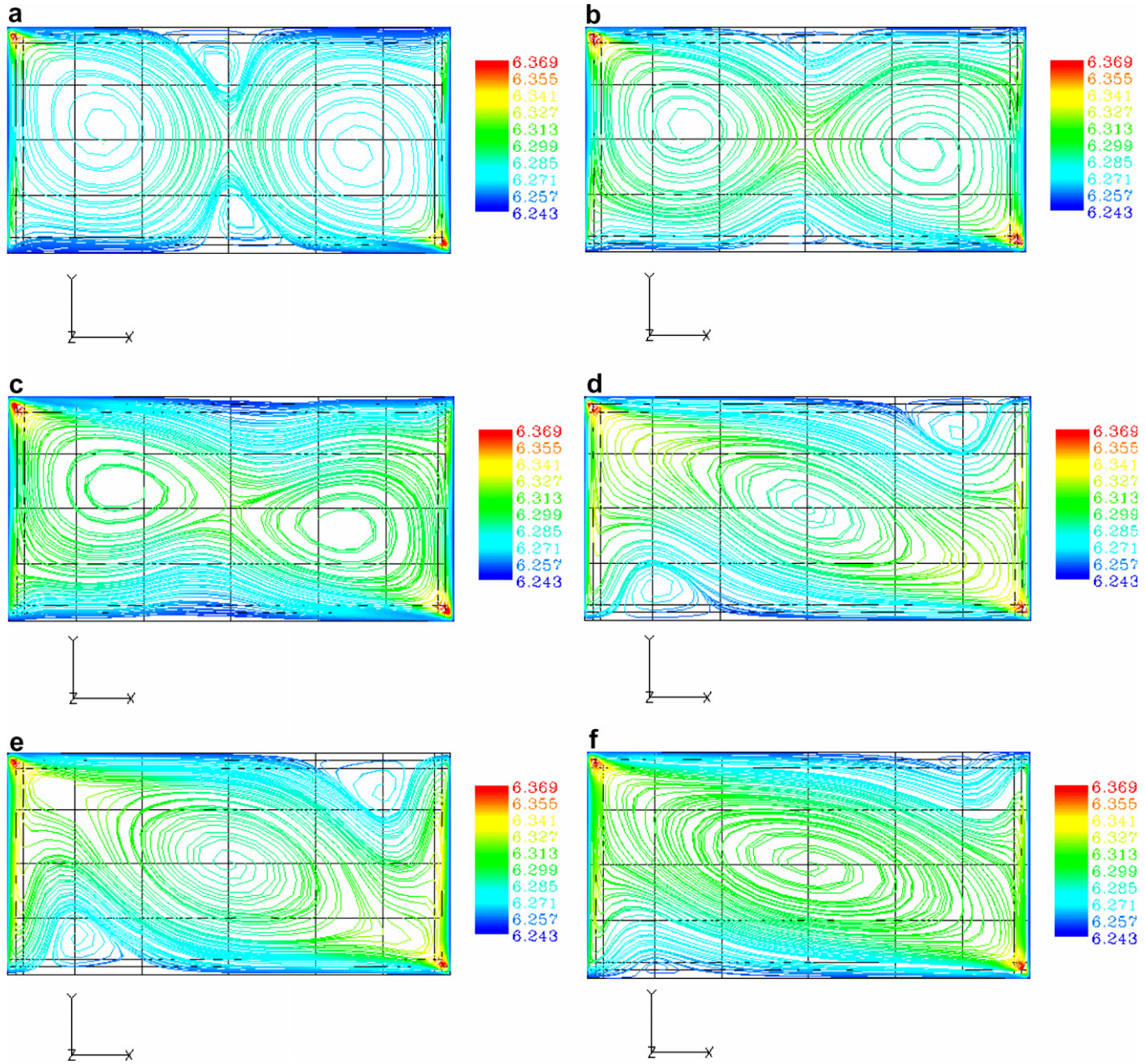

Fig. 3. Flow evolution for $Re = 700$: (a) $t = 12$; (b) $t = 27$; (c) $t = 30$; (d) $t = 33$; (e) $t = 37$, (f) $t = 59$. (For interpretation of the references to color in this figure legend, the reader is referred to the web version of this article.)

of 700, have more strength for a higher Reynolds number and thus, they are larger in size at steady state.

The heat generation by viscous dissipation leads to a local temperature increase near the walls. The higher temperature fluid initially forms the two temperature vortices which combine later. Viscous heating plays an important role in the dynamics of fluids with strongly temperature-dependent density because of the coupling between the energy and momentum equations. When the temperature gradients induced by viscous heating are very pronounced, local instabilities may occur and the triggering of secondary flows is possible. This effect will be discussed in Part II [24] in details.

3.2. Reynolds number effect

For a higher Reynolds number flow, the viscous dissipation is lower, which leads to a lower spatially averaged temperature in the domain. Consequently, the spatially averaged pressure also decreases for a higher Reynolds number. Fig. 4 presents the temporal evolution of the spatially averaged pressure $\overline{P}$, for different Reynolds numbers at $\Gamma = 1.955$ and $Ma = 0.4$. It was discussed earlier that the two initial vortices do not combine to form a single vortex for flows with $Re \leqslant 400$. The $\overline{P}$ vs. time curve for $Re = 400$, is therefore quite smoother compared to that for $Re > 400$. The fluctuating parts in the curves for $Re > 400$, represent

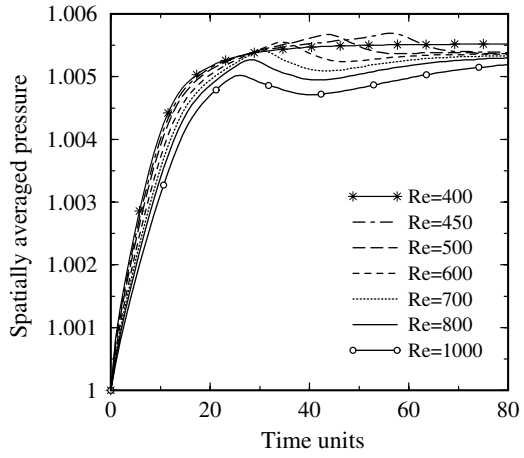

Fig. 4. Temporal evolution of the spatially averaged pressure for various Reynolds numbers with $\Gamma = 1.955$ and $Ma = 0.4$.

the time periods when the phenomenon of merging of the two initial vortices into one takes place. Because the steady state for a low Reynolds number ($Re \leqslant 400$) flow, is the two-vortex stage itself, the flow becomes stable or reaches equilibrium earlier compared to a higher Reynolds number ($Re > 400$) flow.

Now, let us compare only the flows with Reynolds numbers ranging from 450 to 1000, that is the Reynolds numbers showing a single major vortex at steady state. In this particular range, it is observed that "for a flow with higher Reynolds number, though the formation of single vortex is earlier compared to that with lower Reynolds number, the steady state is achieved later". This statement has two parts: first dealing with the time of formation of a single vortex and second dealing with the time of attaining steady state. Regarding the first part of the statement, because the two vortices formed initially are moving in the same direction, the outer layers of the vortices try to merge in order to gain stability. As a result, the friction between the layers of fluid decreases which decreases the heat dissipated and therefore the rate of build-up of spatially averaged temperature decreases. This leads to the decrease in the preliminary upsurge of the spatially averaged pressure. Notice for Reynolds numbers ranging from 450 to 1000, that after an initial build up in the spatially averaged pressure $\overline{P}$, there is a point in time for every Reynolds number where the rate of increase of the spatial average of pressure slows down. This is the time when the two vortices start coming closer which would eventually lead to the merging of the two vortices. After the vortices completely merge, giving rise to a single vortex, the friction between the layers of the fluid has a sudden decrease and therefore the viscous dissipation decreases and again, this decrease is reflected in the spatially averaged temperature and therefore in the spatially averaged pressure. For a higher Reynolds number flow, the viscous friction between the layers of fluid in the domain is less. Therefore, less work is required to merge the two vortices into one and they combine earlier. The sharp peak in the $\overline{P}$ vs. time curve shifts towards smaller times as Reynolds number increases, indicating that for a higher Reynolds number in the range of $450 \leqslant Re \leqslant 1000$, the formation of a single vortex is earlier.

Because of a higher Reynolds number, the flow remains unstable for a longer time compared to a lower Reynolds number flow. This can be recognized from the $\overline{P}$ curves for different Reynolds numbers. When the spatially averaged pressure becomes constant with time, this is the time of entering the steady state regime. Thus, the second part of the above statement is verified, that is, in the range of Reynolds numbers with a single vortex stage, (i.e. $450 \leqslant Re \leqslant 1000$), for higher Reynolds numbers, the steady state is achieved later.

3.3. Aspect ratio effect

In the previous subsection, the effect of Reynolds number on flow patterns for one particular aspect ratio was discussed. It was seen that for an aspect ratio of 1.955, when simulations are run for flows with different Reynolds numbers, the lowest Reynolds number at which a single vortex steady state is obtained is 450. In this subsection, the effect of aspect ratio on the flow patterns is investigated. First, the aspect ratio is set to 2.0 and simulations are run for different Reynolds numbers, in order to find the lowest Reynolds number at which a single vortex steady state is obtained. These cases are simulated for $Ma = 0.4$. The significance of $\Gamma = 2.0$ stems from the observation that the initial vortices that are formed near the walls tend to grow to circular shapes bounded by the stationary walls. At $\Gamma = 2.0$, each vortex can extend to the center of the cavity to gain a circular shape inside a square box covering half of the domain. As a result, for $\Gamma = 2.0$, the chances of direct interactions between two vortex should be noticeably smaller than that in the case with $\Gamma = 1.955$.

Simulations for larger Reynolds numbers for aspect ratio of 2.0 show that a single vortex steady state does not appear until a Reynolds number as high as 1400. At $Re = 1500$, a single vortex stage is seen at steady state. As discussed earlier in detail, the two vortices formed initially in the rectangular cavity, tend to merge in order to gain stability. It is easier for the two smaller vortices in the center to combine together owing to larger space available, than to move towards the corners of the cavity which would eventually lead to the combination of the two larger vortices into one. (This results in a three-vortex situation which will be discussed later in this subsection.) Also, because of a higher Γ, the two vortices formed initially, have to travel more to come close enough. So, in order to merge, more vortex strength, provided by a higher Reynolds number, is required. As a result, the lowest Reynolds number which gives a single vortex steady state, would be higher for a higher Γ.

If Γ is increased steadily from 1.5 to 2.0, the lowest Re at which a single vortex stage appears also increases steadily. However, as Γ approaches 2.0, i.e. at $\Gamma = 1.955$, the Re at

which the first appearance of single vortex steady state occurs, is interestingly very low compared to that for $\Gamma = 2.0$. A modest increase of approximately 2.2% (i.e. from 1.955 to 2.0) in Γ leads to a difference of about 230% in Reynolds number (450–1500) [3]. This shows that a very small change in the aspect ratio can cause vigorous changes in flow patterns, and suggests that the effect of Reynolds number is different for high and low aspect ratios.

In Fig. 5, the variation of the time derivative of spatially averaged pressure, i.e. $\frac{d\overline{P}}{dt}$, is shown as a function of time. This derivative is chosen here instead of $\overline{P}$, to magnify the changes occurred at $Re = 1500$. It can be easily verified from the figure that there is a drastic change in the curve for $Re = 1500$ compared to the smooth curves for the lower Reynolds numbers. The fluctuation in the curve for $Re = 1500$ is exactly during the time when the two vortices merge into one. Further simulations showed that, for aspect ratio 2.5, the vortices do not combine at a Reynolds number as high as 3200. This again verifies the conclusion that, a very small change in the aspect ratio can cause vigorous changes in flow patterns.

The time of merging of the two vortices into one during flow evolution also depends on the aspect ratio. To elaborate, for $Re = 700$ and $Ma = 0.3$, we consider results for various aspect ratios. A change in Γ of about 0.2% (i.e. from $\Gamma = 1.955$ to $\Gamma = 1.96$) brings about a 3% change in the time of combination of the two vortices into one. For $\Gamma = 1.5$, a single vortex stage is seen at about 9 time units, while for $\Gamma = 1.955$, this stage is not seen till 30 time units. There is a major difference of time period of combination of two vortices into a single vortex stage for these two aspect ratios. Here, a 30% difference in aspect ratios, has brought almost a 230% difference in the time of combination of the two vortices into one. Thus, the percentage increase in the time period required for the two vortices to combine is approximately 8 times the percentage increase in the aspect ratios. Some of the other time periods of combination of two-vortices into one are shown in Table 1. It is obvious from the table that as the aspect ratio

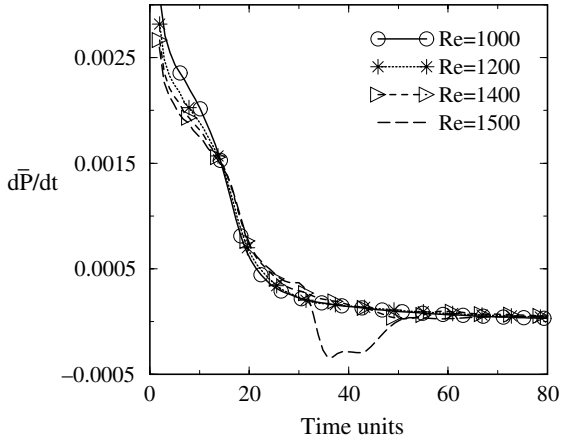

Fig. 5. Comparison of $\frac{d\overline{P}}{dt}$ for different Reynolds numbers when $\Gamma = 2.0$.

Table 1
Combination time for primary vortices for different aspect ratios

Γ	1.0	1.5	1.85	1.955	2.0
Combination time	5	9	16	30	NA

increases between 1.0 and 2.0, the time of combination of two-vortices into one increases. However, it is interesting to see that, as we approach $\Gamma = 2.0$, a smaller change in Γ brings about a larger change in the time of combination. The reason for this is the tendency of a vortex to stay circular. A square cavity is better suited for a flow field to form into a circular vortex compared to a rectangular cavity. So as the aspect ratio increases from 1.0 to 1.5, it becomes harder for the vortices to combine and, therefore, they take more time (or a higher Reynolds number) to combine. A rectangular cavity with an aspect ratio of 2.0, acts like two square cavities and, therefore, it is easier for a two-vortex stage to stay as compared to a cavity with $1.5 < \Gamma < 2$.

Fig. 6 shows the steady state topologies for cases with the same Reynolds number but different aspect ratios. (Streamlines are colored by v-velocity in the figure.) For an aspect ratio up to 1.955, the steady state obtained is a single vortex stage. For a higher aspect ratio of 2.0, during flow evolution, the single vortex stage is never achieved. For $\Gamma \geqslant 2$, it is easier for the two smaller vortices in the center to combine with each other, rather than to move towards the corners of the cavity. Because of a very high aspect ratio, that is a very large distance between the two moving walls guiding the flow, the two larger vortices formed in the beginning are also not close enough to combine. With the passage of time, the vortices gain more and more strength, and tend to increase in size. But due to the inborn tendency of a vortex to stay round, the two vortices can elongate only up to a certain limit. The two smaller initial vortices seen in the center of the cavity near the stationary walls combine for a higher aspect ratio of 2.5. Therefore, there is the formation of one more vortex in the center of the cavity which is again guided by the coupled effects of the moving vortices. This steady state is called a three-vortex stage (see Fig. 6f).

3.4. Mach number effect

A study on Mach numbers ranging from 0.1 to 0.4 for a Reynolds number of 700 and aspect ratio of 1.955 is undertaken. The Mach number is changed by varying the initial temperature, as listed in Table 2. The u velocity plots along the horizontal centreline, i.e. the line $y = 0.5$, and vertical centerline, i.e. the line $x = 0.978$, (Figs. 7a and 8a), show that there is no effect of Mach number on the velocity components. The u velocity is zero at the walls and maximum in magnitude in the outer layers of fluid forming the vortex. The v velocity, (not shown) is zero at the stationary or horizontal walls and maximum in magnitude along the moving

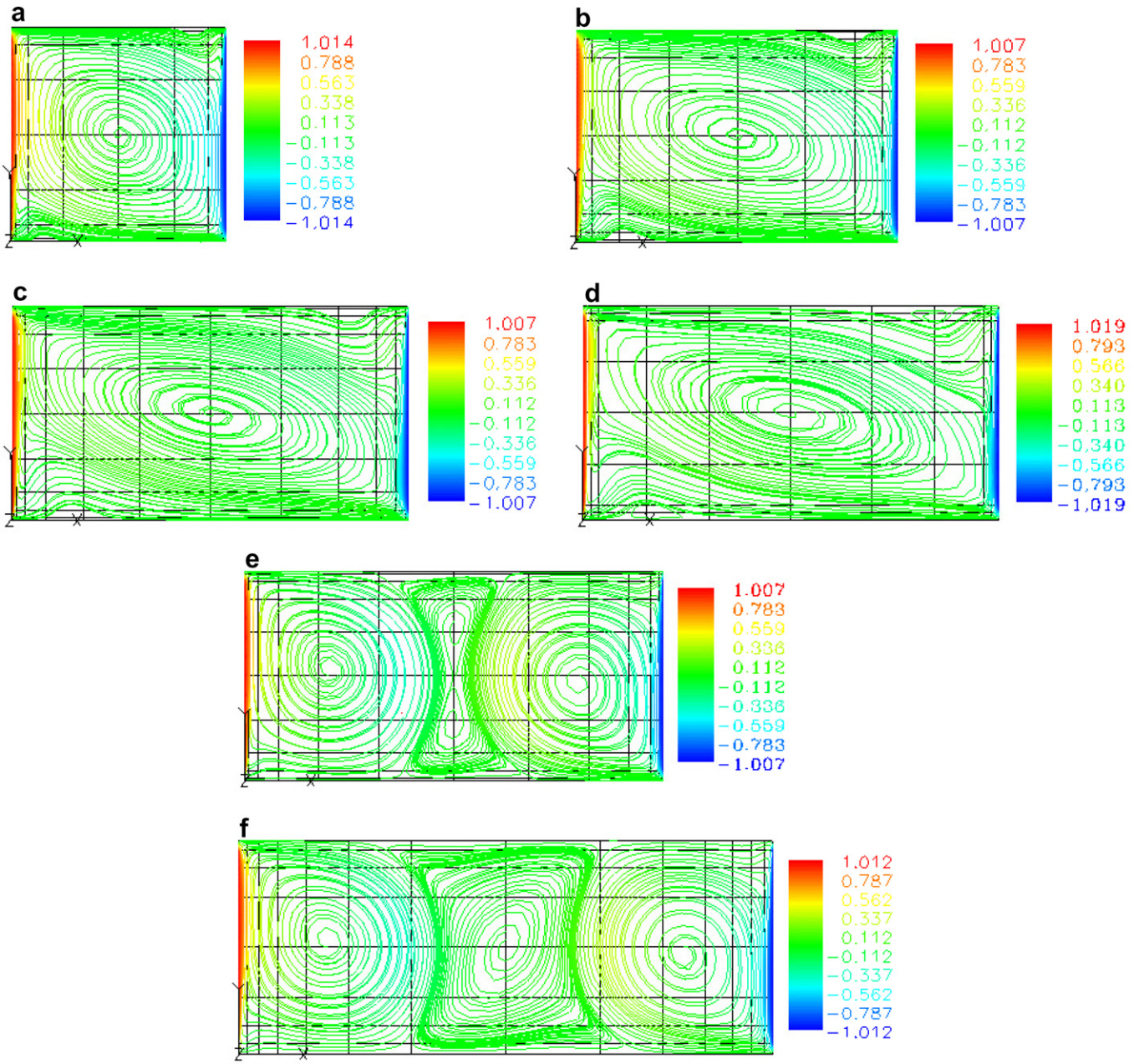

Fig. 6. Streamlines at steady state for $Re = 700$: (a) $\Gamma = 1.0$; (b) $\Gamma = 1.5$; (c) $\Gamma = 1.85$; (d) $\Gamma = 1.955$; (e) $\Gamma = 2.0$; (f) $\Gamma = 2.5$. (For interpretation of the references to color in this figure legend, the reader is referred to the web version of this article.)

Table 2
Values of T_i corresponding to Ma

Ma	0.1	0.2	0.3	0.4
T_i	100.0	25.0	11.11	6.25

or vertical walls. Near the moving walls, the velocity gradients are high.

The temperatures at steady steady state, normalized by the initial temperatures are compared in Figs. 7(b) and 8b. The compressibility effects increase with an increase in the Mach number and, therefore, $Ma = 0.4$ shows the highest differences in the temperature fields. The flow regions having the maximum velocity gradients experience the highest viscous dissipation and thus the maximum temperature. A close examination of Fig. 7b reveals that for $Ma = 0.4$ the minimum temperature occurs at the center of the elliptical vortex. In contrast, along the vertical centerline, the temperature at the center of the vortex is maximum. The moving walls provide the driving force for the vortex. In the horizontal direction, because the velocity at the center of a vortex is minimum, the friction between the layers of fluids is minimum. The heat dissipated, therefore, is less and so is the temperature. The temperature is seen to shoot up near the moving walls. The viscous friction near the moving walls is the highest compared to

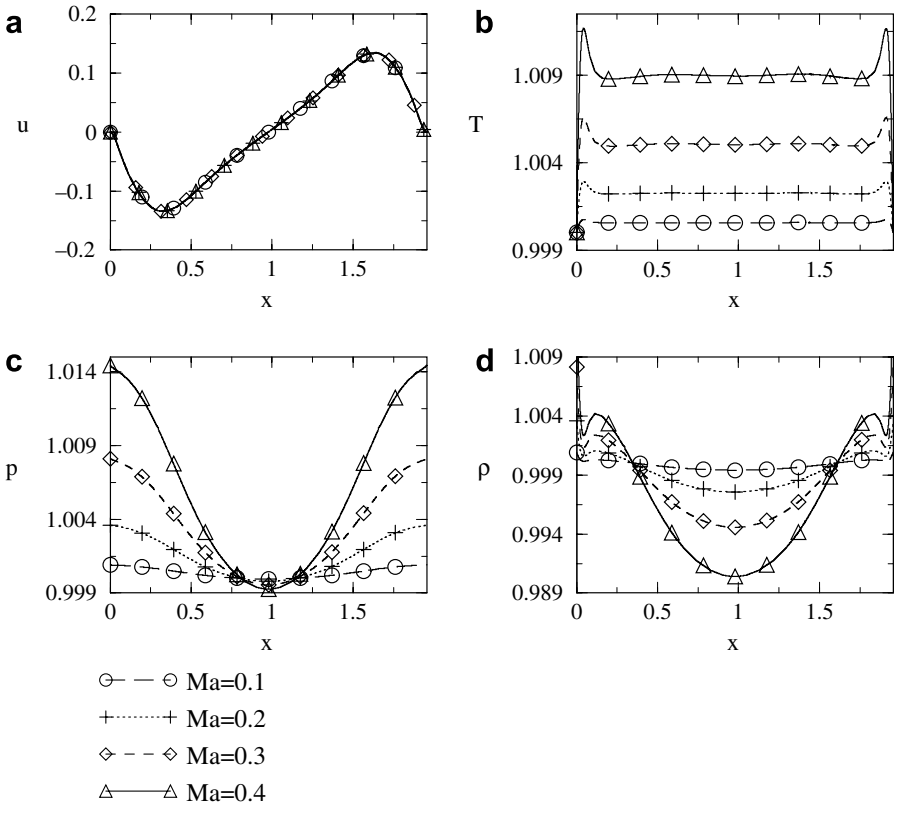

Fig. 7. Effect of Mach number on the flow parameters along the horizontal centerline $y = 0.5$.

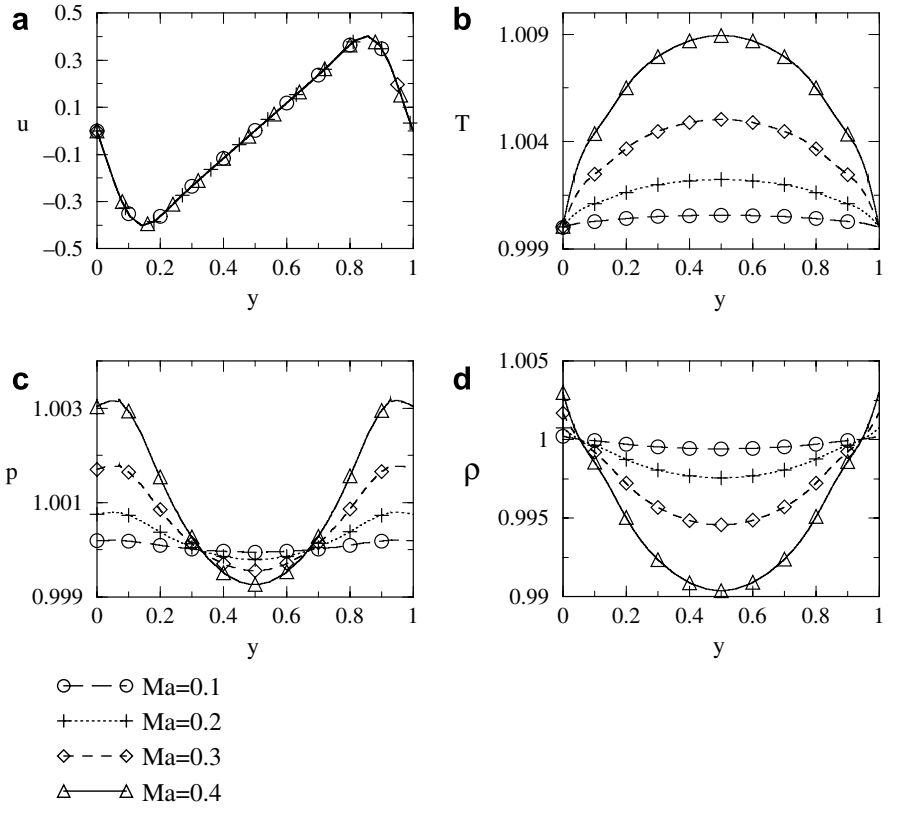

Fig. 8. Effect of Mach number on the flow parameters along the vertical centerline $x = 0.978$.

any other part in the domain because of high velocity gradients. Therefore, the high temperature outside of the vortex along the horizontal centerline can be attributed to the v velocity of the moving walls.

The compressibility effects on local pressure near the moving walls and in the center of the large vortex are visualized by comparing the pressure along the horizontal centerline (Fig. 7c) and the vertical centerline (Fig. 8c). The local pressures for different Mach numbers are compared after normalizing them with the respective initial pressures. It is seen that pressure is minimum at the center of the vortex and maximum on the outer edges of the vortex. This can be attributed to the centrifugal force of the rotating vortex. This difference in pressures at the center and near the outer edges is higher for a higher Ma because of higher compressibility effects. The pressure is higher near the moving walls compared to the stationary walls, consistently with the behavior of the temperature. The spatial average of density in the entire cavity is constant due to the conservation of mass. The density along the horizontal centerline is plotted in Fig. 7d and along the vertical centerline in Fig. 8d. The plots suggest that the center of the vortex is the place with the minimum density. This can again be attributed to the centripetal force of the rotating vortex. Due to the centripetal force, fluid is pushed towards the periphery of the vortex and, therefore, the density at the center of a vortex is minimum. There is a sharp increase in density at the moving wall as seen in Fig. 7d. This sharp increase in density can be attributed to the sharp decrease in temperature at this location. As expected compressibility effects are more pronounced for $Ma = 0.4$. Nearly 1% variation in density is observed at this Mach number.

3.5. Boundary layer study

Next, a detailed study on the formation of velocity and thermal boundary layers along the walls of the domain and the effects of Reynolds number and Mach number on the thicknesses of the boundary layers is provided. The flow field close to the walls can be compared to flow over a flat plate. There is a formation of velocity boundary layer along the walls. A u-velocity boundary layer is seen on horizontal walls and a v-velocity boundary layer is observed on vertical walls. Shear stresses in the boundary layer dissipate some kinetic energy into heat and alter the temperature of the fluid. Thus, the velocity field in the domain gives rise to a thermal boundary layer.

In order to provide a comparison with theory, the system composed of one of the moving walls of the cavity against fluid is assumed to be comparable to the system of laminar flow over a flat plate at zero angle of incidence. The numerical model involving the comparison of boundary layers is the left wall which is moving in the negative y direction and the corresponding theoretical model is that of the flow over a flat plate in the positive y direction (Fig. 9). The flow inside a two-sided lid-driven cavity with a Reynolds number of 700 is considered and the thermal

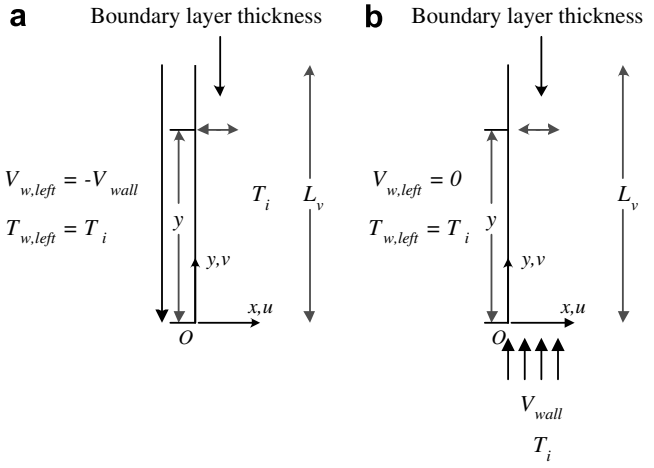

Fig. 9. Schematic diagram of: (a) numerical and (b) theoretical models for comparison of the boundary layers.

and velocity boundary layer thicknesses at the moving walls are found. The Mach number is 0.1, such that the flow can be assumed incompressible. The thermal and velocity boundary layer thicknesses for the incompressible flow over a flat plate are obtained from the theory for the same Reynolds number of 700. These two sets of velocity and thermal boundary layers are then compared to numerical results at the horizontal centerline ($y = 0.5$) near the left moving wall ($x = 0$) of the cavity.

For comparison with theory, we consider the Blasius solution which deals with laminar incompressible boundary layer around a stationary flat plate. Let δ_V and δ_T denote the velocity and temperature boundary layers thicknesses, respectively. The Blasius equations giving the orders of δ_V and δ_T for $Pr \ll 1$ at a distance y from the leading edge of the flat plate are [29]

$$\delta_V \sim Re^{-\frac{1}{2}}y, \quad \delta_T \sim Re^{-\frac{1}{2}}Pr^{-\frac{1}{2}}y. \tag{9}$$

On a flat plate, suppose the line $(0, y)$, the velocity and thermal boundary layer thicknesses are calculated by the similarity solution and Pohlhausen's experimental results. By the similarity solution available for incompressible boundary layer on a flat plate with $Pr > 0.5$,

$$\delta_V = 4.92Re^{-\frac{1}{2}}y, \quad \delta_T = 0.332Re^{-\frac{1}{2}}Pr^{-\frac{1}{3}}y. \tag{10}$$

These equations yield $\delta_V = 0.093$ and $\delta_T = 0.034$ theoretically which are close to the numerically obtained respective values of 0.087 and 0.044. Thus, it is found that the thermal and velocity boundary layer thicknesses obtained numerically for our model are of the same order of magnitude as the theoretical respective boundary layer thicknesses for a flat plate in incompressible flows. The difference of about 7% for the velocity boundary layer is because the comparison of the numerical results is made with a flat plate and it is assumed that there are no other secondary flows present. However, for our case, near the $y = 0$ corner, there is flow in the x-direction. The larger difference, about 30%, for the thermal boundary layer is also not unreason-

able because of the physical differences in the two systems. The theory considers a flat plate at T_i exposed to a flow of gas at a different temperature, whereas in the numerical simulation the temperature difference arises from viscous dissipation.

Fig. 10 shows the variation of various boundary layers with Reynolds number. A lower Reynolds number, keeping density and velocity constant, implies employing a higher viscosity. Fig. 10a shows that the magnitude of $\frac{dv}{dx}$ is smaller for a lower Reynolds number. Thus the velocity boundary layer thickness increases for a lower Reynolds number. Higher viscosity also means higher resistance and therefore higher friction between the layers of a fluid. Thus, there is a greater amount of viscous dissipation which leads to a larger thickness of the thermal boundary layer. The higher the temperature, the lower the density, therefore, the density at the boundary follows an inverse trend as temperature.

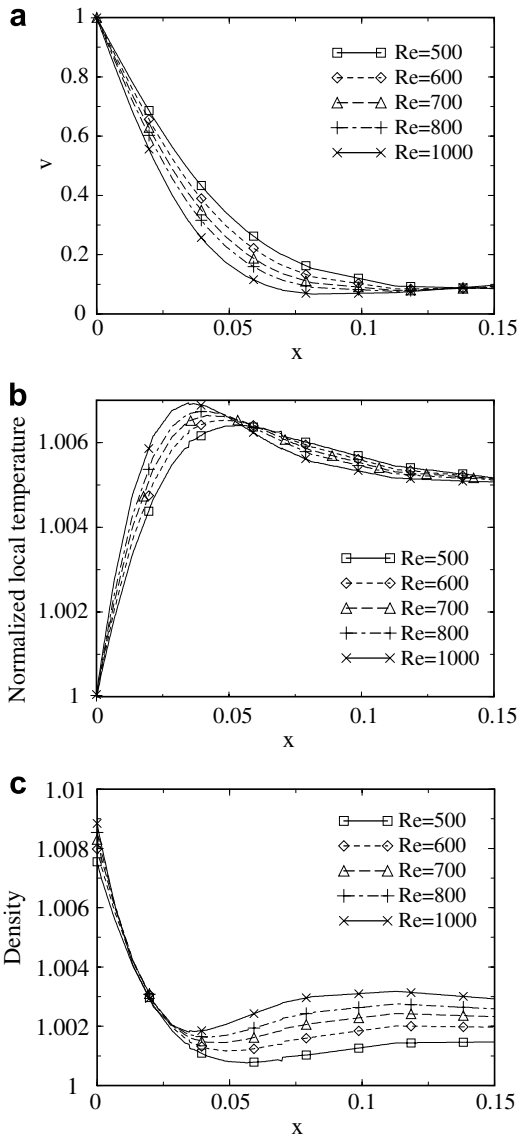

Fig. 10. Effect of Reynolds number on boundary layers: (a) velocity boundary layer; (b) temperature boundary layer and (c) density boundary layer.

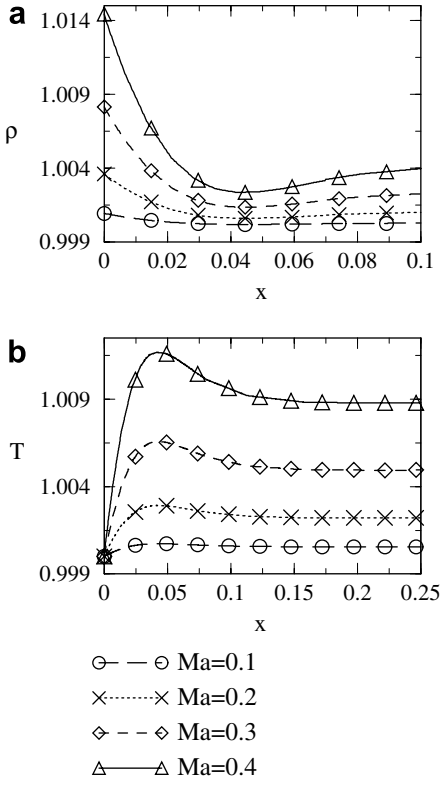

Fig. 11. Effect of Mach number on boundary layer: (a) density boundary layer and (b) temperature boundary layer.

From the numerical results, it is inferred that as the Reynolds number increases from 450 to 1000, the velocity boundary layer thickness and the thermal boundary layer thickness decrease by about 35%. From Eq. (10), this percentage decrease in the velocity and thermal boundary layers thicknesses is 33%.

The effects of Mach number on density and temperature boundary layers are shown in Fig. 11. There is no appreciable effect of Mach number on the velocity boundary layer. The effect of Mach number on boundary layer is studied along the line $y = 0.5$ near the left moving, i.e. $x = 0$, wall. The temperatures at steady state, normalized by the initial temperatures are compared. The differences in temperature and density boundary layers for different Mach numbers are within 1% and suggest small compressibility effects in the cavity flow for $Ma \leqslant 0.4$.

4. Conclusions

The viscous, compressible flow in a two-dimensional lid-driven cavity is studied numerically using a Chebyshev multi-domain spectral element method. Resolution study is conducted and grid independence, convergence in time as well as agreement with published results is achieved. Viscous dissipation leads to the increase of the spatially averaged temperature and pressure in the domain. When the heat transfer from the walls balances the viscous dissipation, the system reaches equilibrium and steady state is

achieved. This is when the spatial averages of pressure and temperature become constant.

Due to the movement of walls, two vortices are formed near the moving walls. There is also a formation of two smaller vortices in the middle of the domain, near the stationary walls, due to the inherent tendency of the two bigger vortices formed by the moving walls to stay circular. This is the steady state flow for a Reynolds number less than 400 for an aspect ratio of 1.955. The direction of rotation of the two bigger vortices is according to the respective moving walls which direct them, i.e. clockwise for the cavity in this study, but the direction of rotation of the two smaller vortices is counter-clockwise. For higher Reynolds numbers, the two-vortex stage is not a stable one. The two vortices merge in the end giving rise to a single stronger elliptical vortex. In the range of Reynolds numbers higher than 400, at higher Reynolds numbers, the time period of formation of a single vortex is earlier compared to that at a lower Reynolds number. Also, for a higher Reynolds number case, the flow enters the steady state regime later compared to a lower Reynolds number case. There is a decrease in the thicknesses of the velocity and temperature boundary layers with an increase in Reynolds number. The thicknesses of these boundary layers for a Mach number of 0.1 obtained numerically, are of the same order of magnitude as those obtained from the theory for incompressible flow on a flat plate. A very small change in the aspect ratio could bring vigorous changes in flow patterns. The single-vortex steady state is seen for a Reynolds number as low as 450 for an aspect ratio of 1.955. But this stage does not appear for a Reynolds number as high as 1400 for an aspect ratio of 2.0. For a very high aspect ratio, e.g. 2.5, a three-vortex stage is observed at steady state.

Acknowledgements

This work was supported in part by the US Office of Naval Research and the National Science Foundation.

References

[1] O.R. Burggraf, Analytical and numerical studies of the structure of steady separated flows, J. Fluid Mech. 24 (1966) 113.
[2] J.R. Koseff, R.L. Street, The lid-driven cavity flow: a synthesis of qualitative and quantitative observations, J. Fluid Eng. 106 (1984) 390.
[3] H.C. Kuhlmann, M. Wanschura, H.J. Rath, Flow in two-sided lid-driven cavities: non-uniqueness, instabilities, and cellular structures, J. Fluid Mech. 336 (1997) 267–299.
[4] H.C. Kuhlmann, M. Wanschura, H.J. Rath, Elliptic instability in two-sided lid-driven cavity flow, Eur. J. Mech. B/Fluid 17 (4) (1998) 561–569.
[5] P.N. Shankar, M.D. Deshpande, Fluid mechanics in the driven cavity, Annu. Rev. Fluid Mech. 32 (2000) 92.
[6] S. Albensoeder, H.C. Kuhlmann, Accurate lid-driven three-dimensional cavity flow, J. Comput. Phys. 206 (2005) 536–558.
[7] F. Pan, A. Acrivos, Steady flows in rectangular cavities, J. Fluid Mech. 28 (1967) 643.
[8] A.K. Prasad, J.R. Koseff, Reynolds number and end-wall effects on a lid-driven cavity flow, Phys. Fluid A. 1 (1989) 208.
[9] V.Y.A. Bogatyrev, A.V. Gorin, End effects in rectangular cavities, Fluid Mech. – Soviet Res. 7 (1978) 101.
[10] J.R. Koseff, R.L. Street, Visualization studies of a shear driven three-dimensional recirculating flow, J. Fluid Eng. 106 (1984) 21.
[11] J.R. Koseff, R.L. Street, On endwall effects in a lid-driven cavity flow, J. Fluid Eng. 106 (1984) 385.
[12] J.W. Goodrich, K. Gustafson, K. Halasi, Hopf bifurcation in the driven cavity, J. Comput. Phy. 90 (1990) 219.
[13] J. Shen, Hopf bifurcation of the unsteady regularized driven cavity flow, J. Comput. Phys. 95 (1991) 228.
[14] C.K. Aidun, N.G. Triantafillopoulos, J.D. Benson, Global stability of a lid-driven cavity with through-flow: flow visualization studies, Phys. Fluids A. 3 (1991) 2081.
[15] J.D. Benson, C.K. Aidun, Transition to unsteady non-periodic state in a through-flow lid-driven cavity, Phys. Fluids A. 4 (1992) 2316.
[16] P.N. Shankar, The eddy structure in Stokes flow in a cavity, J. Fluid Mech. 250 (1993) 371.
[17] R. Srinivasan, Accurate solutions for steady plane flow in the driven cavity, Math. Phys. 46 (1995) 524.
[18] M.M. Gupta, R.P. Manohar, B. Noble, Nature of viscous flows near sharp corners, Comput. Fluid 9 (1981) 379.
[19] M.A. Kelmanson, B. Lonsdale, Eddy genesis in the double-lid-driven cavity, Quart. J. Mech. Appl. Math. 49 (1996) 635.
[20] M. Brons, J.N. Hartnack, Streamline topologies near simple degenerate critical points in two-dimensional flow away from boundaries, Phys. Fluid 11 (1999) 314.
[21] H.K. Moffatt, Viscous and resistive eddies near a sharp corner, J. Fluid Mech. 18 (1964) 1.
[22] C. Migeon, A. Texier, G. Pineau, Effects of lid-driven cavity shape on the flow establishment phase, J. Fluid Struct. 14 (2000) 469.
[23] J.L. Guermond, C. Migeon, G. Pineau, L. Quartapelle, Start-up flows in three-dimensional rectangular driven cavity of aspect ratio 1:1:2 at $Re = 1000$, J. Fluid Mech. 450 (2002) 169–199.
[24] P. Shah, B. Rovagnati, F. Mashayek, G.B. Jacobs, Subsonic compressible flow in two-sided lid-driven cavity. Part II: Unequal walls temperatures, Int. J. Heat Mass Transfer, in press, doi:10.1016/j.ijheatmasstransfer.2007.02.029.
[25] D.A. Kopriva, A staggered-grid multidomain spectral method for the compressible Navier–Stokes equations, J. Comp. Phys. 244 (1998) 142–158.
[26] G.B. Jacobs, D.A. Kopriva, F. Mashayek, A comparison of outflow boundary conditions for the multidomain staggered-grid spectral method, Numer. Heat Transfer, Part B. 44 (3) (2003) 225–251.
[27] G.B. Jacobs. Numerical Simulation of two-phase turbulent compressible flows with a multidomain spectral method. Ph.D. Thesis, University of Illinois at Chicago, Chicago, IL, 2003.
[28] P. Gandhi. Numerical investigation of compressible flow in two-sided lid-driven cavity. MS Thesis, University of Illinois at Chicago, Chicago, IL, 2003.
[29] H. Schlichting, Boundary-Layer Theory, seventh ed., McGraw-Hill Book Co, 1979.